Vehicular Connectivity on Complex Trajectories: Roadway-Geometry Aware ISAC Beam-tracking

Xiao Meng, *Graduate Student Member, IEEE*, Fan Liu, *Member, IEEE*, Christos Masouros, *Senior Member, IEEE*, Weijie Yuan, *Member, IEEE*, Qixun Zhang, *Member, IEEE*, and Zhiyong Feng, *Senior Member, IEEE*

Abstract—In this paper, we propose sensing-assisted beamforming designs for vehicles on arbitrarily shaped roads by relying on integrated sensing and communication (ISAC) signalling. Specifically, we aim to address the limitations of conventional ISAC beam-tracking schemes that do not apply to complex road geometries. To improve the tracking accuracy and communication quality of service (QoS) in vehicle to infrastructure (V2I) networks, it is essential to model the complicated roadway geometry. To that end, we impose the curvilinear coordinate system (CCS) in an interacting multiple model extended Kalman filter (IMM-EKF) framework. By doing so, both the position and the motion of the vehicle on a complicated road can be explicitly modeled and precisely tracked attributing to the benefits from the CCS. Furthermore, an optimization problem is formulated to maximize the array gain by dynamically adjusting the array size and thereby controlling the beamwidth, which takes the performance loss caused by beam misalignment into account. Numerical simulations demonstrate that the roadway geometry-aware ISAC beamforming approach outperforms the communication-only-based and ISAC kinematic-only-based technique in tracking performance. Moreover, the effectiveness of the dynamic beamwidth design is also verified by our numerical results.

Index Terms—V2X, integrated sensing and communication, curvilinear coordinate system, beam tracking

I. INTRODUCTION

THE emerging autonomous driving applications will necessitate Ultra-low latency Gbps wireless links to ensure road safety [1]. In addition, centimetre-level positioning information is also essential to correctly make decisions for driving actions [2]. To achieve such goals, vehicle-to-everything (V2X) communication has become one of the key techniques for autonomous driving, of which two potential technologies are widely discussed, namely, dedicated short-range communications (DSRC) [3], [4] and Celluar V2X (C-V2X) [5], [6]. While the two techniques do offer basic V2X functionalities, they fall short of the demanding requirements mentioned above. Indeed, the data rate of DSRC is restricted to 27Mbps, and the vehicular links may become unreliable in high-density and high-mobility scenarios due to the carrier-sense multiple access mechanism employed [5]. Moreover, the LTE-based system provides Gbps communication service with the positioning accuracy of tens of meters and at a latency often in excess of 1s [1]. As for the NR-V2X, the relative position information can be obtained by side-link communication. Nevertheless, it remains unclear how to accurately acquire the absolute location in real time [5]. Besides, while the positioning error can be reduced to the centimetre-level with the assistance of global navigation satellite-based systems (GNSS), the refresh rate of the positioning information is rather limited [1]. Real-time localization will necessitate the aid of the roadside wireless network, and low latency Gbps links will require accurate formation and steering of high-gain beams.

Thanks to the recent advances in wireless communications, massive multi-input-multi-output (mMIMO) arrays in conjunction with mmWave technologies offer an opportunity to tackle the aforementioned problems [7], [8]. In particular, the large bandwidth available at mmWave frequency simultaneously provides a high data rate for communication and potentially high range resolution for sensing. Meanwhile, the mMIMO array is able to form "pencil-like" beams accurately steering to the targets of interest, which generates a considerable array gain to compensate for the path-loss incurred by mmWave channels, while enhancing the angle resolution for the sensing functionality. Critically, the channel of mmWave mMIMO system exhibits sparsity, i.e., there are much fewer Non-Line-of-Sight (NLoS) components compared with the sub-6 GHz band, which is particularly favourable for vehicle localization [9]. To fully exploit the above advantages of mmWave and mMIMO technologies, it is natural to equip the V2X network with both communication and sensing capabilities, such that the safety and reliability of automated vehicle operation can be significantly improved, with high-speed links and accurate localization performance. In consideration of all these perspectives, research efforts are well-underway toward the deployment of integrated sensing and communication (ISAC)

X. Meng is with the School of Information and Electronics, Beijing Institute of Technology, Beijing, 100081, China, and is also with the Department of Electrical and Electronic Engineering, Southern University of Science and Technology, Shenzhen 518055, China (email: mengxiao94@bit.edu.cn).

F. Liu and W. Yuan are with the Department of Electrical and Electronic Engineering, Southern University of Science and Technology, Shenzhen 518055, China (email: liuf6@sustech.edu.cn; yuanwj@sustech.edu.cn).

C. Masouros is with the Department of Electronic and Electrical Engineering, University College London, London, WC1E 7JE, UK (e-mail: chris.masouros@ieee.org).

Q. Zhang and Z. Feng are with Key Laboratory of Universal Wireless Communications Ministry of Education, Beijing University of Posts and Telecommunications, Beijing 100876, China (e-mail: zhangqixun@bupt.edu.cn; fengzy@bupt.edu.cn)

This article has been accepted for publication in IEEE Transactions on Wireless Communications. This is the author's version which has not been fully edited and content may change prior to final publication. Citation information: DOI 10.1109/TWC.2023.3250442

2

in V2X networks [10]–[15].

More relevant to this work, a dedicated radar sensor mounted on a roadside unit (RSU) may assist the communication beam training in vehicle-to-infrastructure (V2I) downlink scenarios [10]. By doing so, the direction-finding ability of the radar improves the precision of the beam alignment with significantly reduced beam training overhead, which is however at a cost of extra hardware platform. To further exploit the performance gain provided in ISAC V2X network, a vehicular beamforming approach without any additional sensor was proposed in [11], which employed the echo of mmWave payload signal to sense the location of the vehicles and predictively constructed the beamformer in high mobility scenarios. By applying the matched filter (MF) or other estimation methods, the vehicle's state parameters can be estimated in real-time. Then an EKF approach was applied to estimate the present and predict the future position of the vehicle so that an efficient ISAC-based predictive beamforming design can be attained. On top of that, a message-passing-based algorithm from a Bayesian perspective was proposed in [13] to achieve the same objective. Overall, compared with the traditional beam training schemes and emerging beam tracking schemes [16]–[20], the ISAC-based predictive beamforming algorithm exhibits the following superiorities:

- **Low tracking overhead.** Different from conventional tracking techniques in [16]–[20], the dedicated pilot is not required in the transmission frame, which benefits from lower latency and continuous data transmission and removes the need for CSI feedback and the associated quantization and feedback errors.
- **Significant matched-filtering gain.** Through ISAC signalling, the whole transmission frame can be used for simultaneous data transmission and sensing, which leads to a higher gain for matched-filtering processing, compared with the conventional beam training/tracking approaches relying on pilots only. The higher matched-filtering gain improves the sensing performance and makes it easy to construct beams accurately pointed to the vehicular user (VU), thus to provide reliable communication service.
- **Two dimensional localization.** In contrast to conventional approaches operated in the angular domain only, ISAC-based schemes offer additional range information which significantly improves the accuracy of localization.

Although numerous studies on ISAC-enabled V2X networks have already been reported in the literature, there are still quite a lot of critical challenges that prevent the practical implementation, where one important issue is the over-simplified assumptions adopted. While the beam training schemes do not need the prior information of the channel state, the beam tracking algorithms often assume that the targets move around the RSU at a constant absolute velocity [16], [17] or the target is located at a given angle by treating the variation caused by the movement as noise [18], [20], which is obviously mismatched with the realistic scenarios. More importantly, in many existing ISAC-based V2X schemes, the vehicle is assumed to drive on a straight road parallel to the antenna array, which represents a corner case and cannot cover the broader

scenarios [11]–[13]. Accordingly, the kinematic model in the existing treatise and the resultant EKF-based beam tracking algorithm only work under limited roadway geometries. The complicated trajectories may impair the precision of sensing and prediction, which further lead to a low communication rate due to beam misalignment.

In light of the above, we propose a novel sensing-assisted predictive beamforming scheme in V2I networks that is able to operate on arbitrarily shaped roads, by employing a curvilinear coordinate system (CCS) [21]. To further model the complicated driving behavior of the vehicles, multiple kinematic models are taken into consideration. For clarity, the contribution of this paper can be summarized as follows:

- **ISAC-based predictive beamforming for arbitrarily shaped road.** Inspired by [21]–[23], we model the complicated roadway geometry as a CCS and reveal its relationship with the Cartesian and the polar coordinate systems used for sensing, which facilitates beam tracking for the vehicle with uniform velocity.
- **Interacting multiple model (IMM) based beamforming and vehicle maneuver recognition.** Based on the CCS, we further consider a scenario where the vehicle intermittently changes its lane. By applying the IMM filter [24], a more reliable tracking process is established and the maneuver of the vehicle can be readily identified.
- **Dynamic beamwidth (DB) scheme under misalignment probability constraint.** To address the positioning and angle uncertainty of the IMM-EKF-based algorithm, we propose a dynamic beamwidth adjustment algorithm. The proposed algorithm is capable of activating dynamic numbers of antennas to optimize the array gain while guaranteeing that the misalignment probability is lower than a given threshold.

The remainder of this article is organized as follows, Section II introduces the system model and the modeling of CCS, Section III describes the proposed EKF approach and the corresponding IMM filtering, Section IV proposes the dynamic beamwidth algorithm, Section V provides the numerical results, and finally Section VI concludes the paper.

Notations: Unless otherwise specified, matrices are denoted by bold uppercase letters (i.e., $\mathbf{F}$), vectors are represented by bold lowercase letters (i.e., $\mathbf{x}$), and scalars are denoted by normal font (i.e., ρ). $(\cdot)^H$ stands for Hermitian transpose. $\arctan(\cdot)$ and $\arcsin(\cdot)$ denote inverse tangent and inverse sine function in radian. $\lfloor n \rfloor$ denotes the maximum integer no larger than a real number n, and $\mathbb{E}\{\cdot\}$ represents the statistical expectation. $\{x, y\}$ and (s, n) denote the location in the Cartesian coordinate system and the CCS, respectively.

II. System Model

In this paper, we consider a V2I downlink scenario where an RSU equipped with a massive antenna array and working at mmWave frequency servers a single antenna vehicle. The vehicle is assumed to be driven on a road with an arbitrary shape on the x-y plane, and the RSU communicates with the vehicle via Line-of-Sight (LoS) channel. Moreover, a uniform planner array (UPA) with $2M$ columns and N rows is assumed
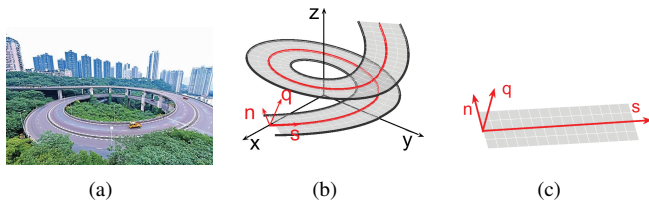
Fig. 1. The Location and motion can be easily modeled in Curvilinear Coordinate system.

Fig. 2. The relationship between the CCS, Cartesian coordinate system and the polar system.

to be deployed at the RSU, which is equally divided into transmit and receive array, i.e., $N_t = N_r = M \times N$. The shape of the road around the RSU is known by importing a map with high precision or acquiring the roadway information from the road designers. Given the page limit, we designate the discussion of the NLoS channel and the road in 3-dimensional models as our future work.

A. Road Geometry Model

Our goal is to track the variation of the position and the motion of the vehicle so that we can use quite a narrow beam to communicate with the vehicle and obtain the high array gain. In contrast to the straight road model considered in [11]–[13], the kinematic equation of the vehicle on a curve road is extremely difficult to be described either in the Cartesian coordinate system or in the polar coordinate system. This motivates us to model the motion of the vehicle on such road in CCS.

1) Basic Concept of Curvilinear Coordinate System: The CCS is characterized in the Euclidean space where a certain number of the coordinate axes are represented based on a curved geometry. As shown in Fig. 1, the complicated road described by x, y, and z in the Cartesian coordinate system can be represented in CCS by using s, n and q. Based on the CCS, the position and motion have more clear meaning compared with that in the Cartesian coordinate system. The s axis represents the dimension that follows the curvature of the arbitrary road, with the value of s denoting the distance travelled along that axis. The n axis is perpendicular to s and the value of n represents the lateral distance from the s-axis. The q axis is perpendicular to s and n and the values of q represent the distance on the height dimension in our scenario. By converting the kinematic description into the roadway-geometry-based CCS, the motion of the vehicle can be easily described in an explicit way.

2) Description of the Curve by Fitting Equations: To set up such a coordinate system under road geometry, we need to first choose a proper method to describe the axis of the new coordinate system. Without the loss of generality, we use the cubic spline interpolation algorithm in this paper to fit the line that runs across the middle of the road by using a set of parametric functions. Accordingly, the new coordinate system can be described by this set of parameters. The cubic spline interpolation algorithm can offer not only a high fitting precision but also continuous second-order derivation, which is a useful property in the state description for our EKF in the following. Besides, since road designers sometimes use the
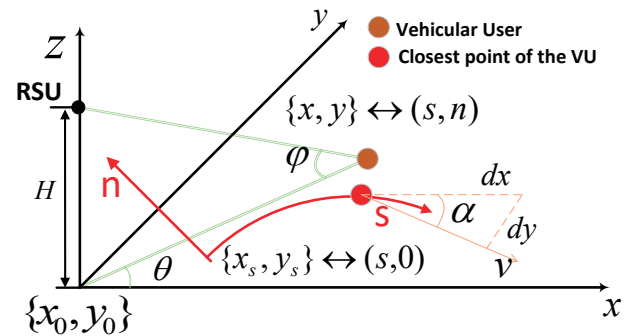
cubic spline interpolation algorithm to describe the curve, the fitting algorithm can achieve fairly high accuracy if the design of the road is available.

In order to apply the cubic spline interpolation algorithm, the curve of interest is divided into I segments by $I+1$ control points, which include the start point and the endpoint. Any point on the curve in the i-th segment between the i-th control point and the $(i+1)$-th control point can be described by the following equation:

$$[x_s, y_s, s]^T = [\boldsymbol{a}_i, \boldsymbol{b}_i, \boldsymbol{c}_i]^T [\rho^3, \rho^2, \rho, 1]^T, \qquad (1)$$

where s is the length along the road and also the value on the s axis in the CCS, (x_s, y_s) is the position of the point in the Cartesian coordinate system, $\boldsymbol{a}_i$, $\boldsymbol{b}_i$, $\boldsymbol{c}_i \in \mathbb{R}^{4 \times 1}$ are the parameter sets which calculated by the cubic spline interpolation algorithm in the i-th segment, and ρ is the variable of the parametric functions. This equation implies that any given point on the curve can be simultaneously expressed in the CCS and the Cartesian coordinate system by a certain parameter ρ.

3) Interplay between the Coordinate Systems: In the considered ISAC system, we estimate the classic sensed parameters, such as Doppler frequency and angle of arrival (AoA), which are naturally described in the polar coordinate system. Thus, the relationship between the different coordinate systems should be revealed. Since the conversion between the polar and Cartesian coordinate systems is straightforward, we mainly focus on the relationship between the CCS and the Cartesian coordinate system.

As shown in Fig. 2, the RSU is located at $\{x_0, y_0\}$ with the height being H to give a bird's eye view. The VU is located at $(s, n, 0)$ in the CCS, (θ, φ, d) in the polar coordinate system and $\{x, y, 0\}$ in the Cartesian coordinate system, where θ, φ and d represent the azimuth angle, elevation angle and the distance from the RSU to the VU, respectively. For brevity, we express $(s, n, 0)$ and $\{x, y, 0\}$ as (s, n) and $\{x, y\}$, respectively. The closest point is the projection of the VU on the s axis, which is located at $(s, 0)$ in the CCS and $\{x_s, y_s\}$ in the Cartesian coordinate system. By recalling (1), it is easy to convert this point between the two coordinate systems. By denoting the direction of the road at the closest point as α,

the relationship between the VU and its closest point can be expressed as

$$[x, y] = [x_s, y_s] + n[-\sin\alpha, \cos\alpha]. \tag{2}$$

The direction α can be calculate by $\alpha = \arctan(dy_s/dx_s)$, where dy_s/dx_s can be obtained from (1). Since n is explicitly expressed in the CCS, the conversion from the CCS to the Cartesian coordinate system is straightforward. Moreover, it can be shown in the following part that the reversed conversion from the Cartesian coordinate system to the CCS is not required in any step in the proposed algorithm.

B. Signal Model

As shown in Fig. 3, the RSU transmits the ISAC signal to the vehicle and receives the echo signal from the vehicle simultaneously in our considered ISAC V2I downlink scenario. In each epoch, the RSU tries to construct a beam that steers to the vehicle by applying the predicted angle of the vehicle. To explore how the transmit and receive signal impact the sensing and communication performance, we investigate the signal model in this subsection. Since the initial state of the vehicles can be easily obtained by conventional device-based sensing methods, such as beam training and handoff between the different RSUs, we focus on the signal model of the tracking state at the l-th epoch.
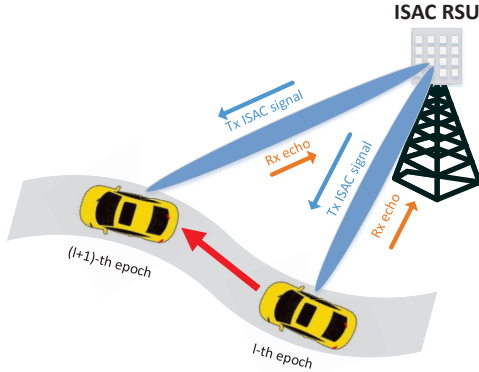

Fig. 3. ISAC V2I scenario model.

1) Communication Signal Model: Let us denote the downlink transmitted ISAC data stream at the l-th epoch and time t as $\bar{s}_l(t)$. The transmit signal can be expressed as

$$\tilde{\mathbf{s}}_l(t) = \sqrt{p_l}\mathbf{f}_l\bar{s}_l(t) \in \mathbb{C}^{N_t \times 1}, \tag{3}$$

where $\mathbf{f}_l$ is the transmit beamforming and p_l is the total transmit power at the RSU. Since we consider an LoS channel between the RSU and the vehicle with a single antenna, the channel vector has the similar form as the steering vector from the RSU to the VU, i. e., $\mathbf{h}_c = \sqrt{\alpha}\mathbf{a}(\theta, \varphi)$, with α being the path-loss. The m-th entry of the array steering vector can be modeled as

$$a(\theta, \varphi)_m = e^{-j\pi(\lfloor\frac{m}{M}\rfloor\sin\varphi\cos\theta + (m-M\lfloor\frac{m}{M}\rfloor)\sin\varphi\sin\theta)}. \tag{4}$$

As we aim to achieve the highest array gain, the transmit beamformer should be designed in the following form, which corresponds to the channel vector,

$$\mathbf{f}_l = \mathbf{a}(\theta_l, \varphi_l) \approx \mathbf{a}(\hat{\theta}_{l|l-1}, \hat{\varphi}_{l|l-1}), \tag{5}$$

where $\hat{\theta}_{l|l-1}$ and $\hat{\varphi}_{l|l-1}$ are the predicted angles at the l-th epoch based on the estimation at the $(l-1)$-th epoch since the real angle is unavailable to the RSU.

The receive signal at the vehicle can be accordingly expressed as

$$r_{c,l}(t) = \sqrt{\alpha_l}\mathbf{a}^H(\theta_l, \varphi_l)\tilde{\mathbf{s}}(t - \tau_{c,l})e^{j2\pi\varrho_{c,l}t} + z_c(t), \tag{6}$$

with $\tau_{c,l}$ and $\varrho_{c,l}$ being the time delay and the Doppler frequency at the vehicle at the l-th epoch, respectively. [1] Assuming the RSU is equipped with omnidirectional antennas, the path-loss can be modeled as [25]

$$\alpha_l(\text{dB}) = 32.4 + 20\log_{10}f_c(\text{MHz}) + (20\times\eta)\log_{10}d_l(\text{km}), \tag{7}$$

with η being the path-loss factor corresponding to the carrier frequency and the electromagnetic propagation environment and we assume $\eta = 1$ in this paper.

2) Radar Signal Model: Compared with the communication signal, the channel matrix should be formulated as cascaded channel vectors, and the Doppler frequency and time delay of the radar signal are doubled due to the round trip of the reflected signal. The power of the reflected signal is not only determined by the round-trip path-loss but also by the radar cross-section (RCS) of the target. Thus, the received signal vector can be expressed in the following form

$$\mathbf{r}_l(t) = \beta_l\mathbf{b}(\theta_l, \varphi_l)\mathbf{a}^H(\theta_l, \varphi_l)\tilde{\mathbf{s}}(t - \tau_l)e^{j2\pi\mu_l t} + \mathbf{z}_r(t), \tag{8}$$

where $\mathbf{z}_r \in \mathbb{C}^{N_r \times 1}$ denotes the complex additive white Gaussian noise with zero mean and variance of σ^2 and β_l, μ_l and τ_l represent the reflection coefficient, the Doppler frequency and the time delay for the RSU. Besides, the receive channel vector $\mathbf{b}(\theta, \varphi)$ has the same form as the transmit channel vector when the number of the receive antenna is the same as the transmit antenna. Based on the radar equation, the reflection coefficient of this ISAC system with standard omnidirectional antennas, which contains the RCS and path-loss, can be modeled as [25]

$$\beta_l = \frac{\lambda\epsilon_l}{(4\pi)^{3/2}d_l^{(2\times\eta)}}, \tag{9}$$

where ϵ_l represents the RCS at the l-th epoch, d_l represents the propagation distance and λ is the wavelength of the carrier, which can be mathematically expressed as $\lambda = f_c/c$ with f_c being the frequency of the carrier and c being the speed of the light. Again, we assume a free space propagation which leads to $\eta = 1$.

III. THE PROPOSED APPROACH

A. Extended Kalman Filter

1) State Evolution Model: To accurately track the position and the reflection coefficient of the vehicle, the kinematic states should be properly modeled. Based on the aforementioned curvilinear coordinate system, the position state and the motion state of the vehicle can be naturally decomposed into two orthogonal directions, namely the longitudinal and lateral directions.

[1]The predicted Doppler frequency and delay can be estimated by the RSU and fed to the VU to alleviate the computational overhead of the VU.

In this paper, we assume that the vehicle is stably driven forward or changed its lane, such that the velocity of the vehicle remains unchanged within a single epoch, and that the change between the two adjacent epochs is regarded as system noise. Therefore, without considering the system noise, the distance and the velocity in the two directions at the l-th epoch can be expressed by $s_l = s_{l-1} + v_{s,l-1}\Delta T$, $n_l = n_{l-1} + v_{n,l-1}\Delta T$, $v_{s,l} = v_{s,l-1}$ and $v_{n,l} = v_{n,l-1}$, where ΔT is the duration of a single epoch. By defining the propagation distance of the signal as

$$d = \sqrt{(x_0 - x)^2 + (y_0 - y)^2 + z_0^2}, \qquad (10)$$

the reflection coefficients in the two adjacent epochs can be expressed as

$$\beta_l = \frac{\lambda\epsilon_l}{(4\pi)^{3/2}d_l^2}, \quad \beta_{l-1} = \frac{\lambda\epsilon_{l-1}}{(4\pi)^{3/2}d_{l-1}^2}, \qquad (11)$$

where $\{x_0, y_0, z_0\}$ and $\{x, y\}$ denote the Cartesian coordinates of the RSU and the vehicle, respectively, and ε_l and ε_{l-1} denote the complex RCS at the l-th epoch and $(l-1)$-th epoch, respectively. The RCS of the vehicle is assumed to be a constant within a short period, i. e., $\varepsilon_l \approx \varepsilon_{l-1}$, corresponding to a Swerling I target model [25]. Therefore, the evolution of the reflection coefficient can be formulated as

$$\beta_l = \beta_{l-1}\frac{\varepsilon_l d_{l-1}^2}{\varepsilon_{l-1}d_l^2} \approx \beta_{l-1}\frac{d_{l-1}^2}{d_l^2}. \qquad (12)$$

The full state evolution model can be accordingly summarized as

$$\begin{cases} s_l = s_{l-1} + v_{s,l-1}\Delta T + \omega_s, \\ v_{s,l} = v_{s,l-1} + \omega_{v_s}, \\ n_l = n_{l-1} + v_{n,l-1}\Delta T + \omega_n, \\ v_{n,l} = v_{n,l-1} + \omega_{v_n}, \\ \beta_l = \beta_{l-1}\frac{d_{l-1}^2}{d_l^2} + \omega_\beta \end{cases} \qquad (13)$$

where ω_s, ω_{v_s}, ω_n, ω_{v_n} and ω_β are the system noise of the state evolution function, which are related to the approximation and systematic error of the description to the system.

Further, we introduce two classic motion models to interpret the behavior of the vehicle. When the vehicle is moving stably on the road at a constant velocity without any turning, we can describe the motion of the vehicle by using s, n, and v_s. In this model, the lateral velocity and its corresponding system noise are considered as $v_s = 0$, $\omega_{v_s} = 0$, which is called lane-keeping (LK). On the other hand, in the lane-changing (LC) model, we describe the motion of the vehicle by taking the lateral velocity v_n into account when the vehicle is changing the lane. By adding such an additional state variable, the maneuver of the vehicle can be described while the additional system noise is also introduced.

2) Radar Measurement Model: Once the RSU receives the echo signal at the l-th epoch, we can first invoke the classic MUltiple SIgnal Classification (MUSIC) algorithm to estimate the AoA, $\hat{\theta}_l$ and $\hat{\varphi}_l$ [26].[2] Then, by employing the Angle and Phase EStimation (APES) algorithm [27], the reflection

[2]The estimated or the predicted AoA can be fed to the VU to construct a receive beamformer when the VU is equipped with an antenna array [11].

coefficient $\hat{\beta}_l$ can also be readily obtained. After that, by constructing the receive beamformer from the estimated AoA, the weighted received signal can be expressed as

$$\tilde{r}_l(t) = \beta_l\mathbf{w}^H(\hat{\theta}_l, \hat{\varphi}_l)\mathbf{b}(\theta_l, \varphi_l)\mathbf{a}^H(\theta_l, \varphi_l)\tilde{\mathbf{s}}(t-\tau_l)e^{j2\pi\mu_l t}+\tilde{z}_r(t), \qquad (14)$$

where $\mathbf{w}^H(\theta_l, \varphi_l)$ is the receive beamforming vector which can be expressed as

$$\mathbf{w}(\hat{\theta}_l, \hat{\varphi}_l) = \sqrt{\frac{1}{N_r}}\mathbf{b}(\hat{\theta}_l, \hat{\varphi}_l). \qquad (15)$$

It should be highlighted that by using the massive MIMO array at the RSU, the transmit and receive beams are sufficiently narrow, such that the inter-beam interference can be omitted for multiple vehicles scenario. This follows from the established mMIMO theory and can be mathematically expressed as follows [9]:

$$|\mathbf{a}^H(\theta_0, \varphi_0)\mathbf{a}(\theta_1, \varphi_1)| \to 0, \forall\theta_0 \neq \theta_1 \text{ or } \varphi_0 \neq \varphi_1, N_t \to \infty. \qquad (16)$$

Then, by employing the matched filter with a delayed and Doppler-shifted counterpart of $s_l(t)$, one can estimate the delay τ_l and the Doppler frequency μ_l, which can be analytically given as

$$\{\hat{\tau}_l, \hat{\mu}_l\} = \arg\max_{\tau,\mu}\left|\int_0^{\Delta T}\tilde{r}_l(t)\bar{s}_l^*(t-\tau)e^{-j2\pi\mu t}\,dt\right|^2. \qquad (17)$$

For the sake of simplicity, we summarize the estimated parameters and the corresponding noise as follows:

$$[\hat{\theta}_l, \hat{\varphi}_l, \hat{\mu}_l, \hat{\tau}_l, \hat{\beta}_l] = [\theta_l, \varphi_l, \frac{2\cos(\varphi)v_{R,l}}{\lambda}, \frac{2d_l}{c}, \beta_l] + \mathbf{z} \qquad (18)$$

where $v_{R,l}$ is the radial velocity which can be expressed as $v_{R,l} = v_{s,l}\cos(\theta - \alpha) + v_{n,l}\sin(\theta - \alpha)$, $\mathbf{z} = [z_\theta, z_\varphi, z_\mu, z_\tau, z_\beta]$ is measurement noise vector.

3) Covariance Matrices Approximation: To better exploit the EKF algorithm, the covariance matrices of the measurement noise should be properly set. Before analyzing the covariance matrices, we first rewrite the received signal in a more compact form to derive the receive signal-to-noise ratio (SNR), which has an explicit impact on the measurement noise, and can be given by

$$\tilde{r}_l(t) = \sqrt{p_l}\beta_l\kappa_{T,l}\kappa_{R,l}\bar{s}_l(t-\tau_l) + \tilde{z}_r(t), \qquad (19)$$

where κ_T and κ_R are the transmit and receive beamforming gains which are defined as

$$\kappa_{R,l} = \sqrt{\frac{1}{N_r}}\left|\mathbf{w}^H(\hat{\theta}_l, \hat{\varphi}_l)\mathbf{b}(\theta_l, \varphi_l)\right| \leq \sqrt{N_r}, \qquad (20)$$

$$\kappa_{T,l} = \sqrt{\frac{1}{N_t}}\left|\mathbf{a}^H(\theta_l, \varphi_l)\mathbf{a}(\hat{\theta}_{l|l-1}, \hat{\varphi}_{l|l-1})\right| \leq \sqrt{N_t}. \qquad (21)$$

Thus, the per antenna receive SNR and the beamformed SNR can be expressed as

$$\rho_0 = \frac{p_l\beta_l^2\kappa_{T,l}^2}{\sigma^2}, \quad \rho_1 = \frac{p_l\beta_l^2\kappa_{T,l}^2\kappa_{R,l}^2}{\sigma^2}. \qquad (22)$$

Since what we actually estimated by applying the MUSIC algorithm are the spatial frequencies $a = \pi\sin\varphi\cos\theta$ and $b = \pi\sin\varphi\sin\theta$, the actual azimuth angle and elevation angle

and the corresponding Cramer-Rao Lower Bound (CRLB) can be calculated by the following equations,

$$\theta = \arctan\left(\frac{b}{a}\right), \qquad \varphi = \arcsin\frac{\sqrt{a^2 + b^2}}{\pi}, \qquad (23)$$

$$\mathbf{C}_{\theta,\varphi} = \begin{bmatrix} \frac{\partial\theta}{\partial a} & \frac{\partial\theta}{\partial b} \\ \frac{\partial\varphi}{\partial a} & \frac{\partial\varphi}{\partial b} \end{bmatrix} \begin{bmatrix} C_a & 0 \\ 0 & C_b \end{bmatrix} \begin{bmatrix} \frac{\partial\theta}{\partial a} & \frac{\partial\theta}{\partial b} \\ \frac{\partial\varphi}{\partial a} & \frac{\partial\varphi}{\partial b} \end{bmatrix}^T, \qquad (24)$$

where the Jacobian matrix is easy to calculate. The CRLB of a and b can be formulated as

$$C_a = C_b = \frac{6}{N_{Sample}^2 N_r \rho_0}, \qquad (25)$$

with N_{sample} being the number of signal samples. As for the reflection coefficient, while the CRLB of the APES algorithm has not been explicitly given, we apply the empirical equation to estimate CRLB of which the approximated error can be verified to be quite small [28]. Thus, we approximate the lower bound of the estimation error of β as

$$C_\beta = \frac{1}{N_{sample} N_r \rho_0}. \qquad (26)$$

The CRLB of estimation for a classic MF algorithm can be directly expressed as [25]

$$C_\tau = \frac{3}{2\pi^2 B_w \chi}, C_\mu = \frac{1}{(2\pi)^2 \Delta T^2 f_s \chi}. \qquad (27)$$

In (27), B_w and f_s denote the bandwidth of the ISAC signal and the sample rate of the analog-digital converter (ADC), respectively, and χ is the output power SNR of the MF with the following definition

$$\chi = \frac{E_s}{N_0} = \frac{P_r \Delta T B_w}{\sigma^2} = \rho_1 \Delta T B_w. \qquad (28)$$

4) Preparation of EKF Procedure: In this subsection, we summarize the state evolution model and the measurement model and then derive the corresponding covariance matrices and Jacobian matrices before showing the standard EKF procedure. Although the nonlinearity of the kinematic model is alleviated by applying the CCS, the nonlinearity of the conversion between the polar coordinate system and the CCS still makes it impossible to directly employ the linear Kalman filter in our system. Thus, we consider an extended Kalman filtering approach that employs the first-order Taylor expansion as the approximation of the nonlinear model. By denoting the state variables and the measurement signal vector as $\mathcal{X} = [s, v_s, n, v_n, \beta]^T$ and $\mathcal{Y} = [\hat{\theta}, \hat{\varphi}, \hat{\mu}, \hat{\tau}, \hat{\beta}]$, respectively, the model derived in (13) and (18) can be recast in compact forms as

$$\begin{cases} \text{State Evolution Model: } \mathcal{X}_l = g(\mathcal{X}_{l-1}) + \boldsymbol{\omega}_l, \\ \text{Measurement Model: } \mathcal{Y}_l = h(\mathcal{X}_l) + \mathbf{z}_l, \end{cases} \qquad (29)$$

where $g(\cdot)$ is defined in (13), with $\boldsymbol{\omega} = [\omega_s, \omega_{v_s}, \omega_n, \omega_{v_n}, \omega_\beta]^T$ being the system noise vector and $h(\cdot)$ is defined in (18) with $\mathbf{z} = [z_\theta, z_\varphi, z_\mu, z_\tau, z_\beta]^T$ being the measurement noise vector.

As considered above, $\boldsymbol{\omega}$ can be modeled as zero-mean Gaussian distributed noise with the covariance matrices being expressed as $\mathbf{Q}_s$ [18], [25]. As for $\mathbf{z}$, the empirical estimation errors of the MUSIC algorithm and the APES algorithm follow the Gaussian distribution while the errors of matched filter are not Gaussian distributed [25]–[27]. However, since the errors show similar distribution with the Gaussian distribution, the EKF may not suffers severe performance loss by regarding these errors as Gaussian. For sake of simplicity, we model the measurement as Gaussian distribution with a covariance matrix $\mathbf{Q}_m$.

$$\mathbf{Q}_s = \begin{bmatrix} \sigma_s^2 & \sigma_{s,v_s}^2 & 0 & 0 & 0 \\ \sigma_{s,v_s}^2 & \sigma_{v_s}^2 & 0 & 0 & 0 \\ 0 & 0 & \sigma_n^2 & \sigma_{n,v_n}^2 & 0 \\ 0 & 0 & \sigma_{n,v_n}^2 & \sigma_{v_n}^2 & 0 \\ 0 & 0 & 0 & 0 & \sigma_\beta^2 \end{bmatrix}, \qquad (30)$$

$$\mathbf{Q}_m = \text{diag}(C_{\theta,\varphi}, C_\tau, C_\mu, C_\beta), \qquad (31)$$

where $\sigma_s, \sigma_{v_s}, \sigma_n, \sigma_{v_n}$, and σ_β denote the variance of the state variables, and σ_{s,v_s} as well as σ_{n,v_n} denote the covariance of velocity and distance. Moreover, the covariance matrix of the system noise can be empirically set by considering the type of the vehicle, the road condition, the frame of the ISAC system, and other relevant factors of the system. To linearize the models, we give the Jacobian matrices for both $g(\mathcal{X})$ and $h(\mathcal{X})$ as

$$\frac{\partial g}{\partial \mathcal{X}} = \begin{bmatrix} 1 & 0 & \Delta T & 0 & 0 \\ 0 & 1 & 0 & \Delta T & 0 \\ 0 & 0 & 1 & 0 & 0 \\ 0 & 0 & 0 & 1 & 0 \\ \frac{\partial\check{\beta}}{\partial s} & \frac{\partial\check{\beta}}{\partial n} & \frac{\partial\check{\beta}}{\partial v_s} & \frac{\partial\check{\beta}}{\partial v_n} & \frac{d^2}{\check{d}^2} \end{bmatrix}, \qquad (32)$$

$$\frac{\partial h}{\partial \mathcal{X}} = \begin{bmatrix} \frac{\partial\theta}{\partial s} & \frac{\partial\theta}{\partial n} & 0 & 0 & 0 \\ \frac{\partial\varphi}{\partial s} & \frac{\partial\varphi}{\partial n} & 0 & 0 & 0 \\ \frac{\partial\mu}{\partial s} & \frac{\partial\mu}{\partial n} & \frac{\partial\mu}{\partial v_s} & \frac{\partial\mu}{\partial v_n} & 0 \\ \frac{\partial\tau}{\partial s} & \frac{\partial\tau}{\partial n} & 0 & 0 & 0 \\ 0 & 0 & 0 & 0 & 1 \end{bmatrix}, \qquad (33)$$

where we omit the time index $l-1$ at the l-th epoch and substitute $(\cdot)_l$ as $(\check{\cdot})$. The derivates in the two matrices can be calculated by recalling the definition of the state evolution model and the measurement model and applying the chain rule. The overall EKF algorithm will be summarized with the IMM algorithm as IMM-EKF scheme in the next subsection.

B. IMM Filtering for Motion Tracking and Reasoning

While the EKF scheme is capable of achieving high accuracy when tracking and predicting the state of the vehicle under a single kinematic model, it may be difficult to generalize to the case where the vehicle may switch among multiple kinematic models. This implies that the motion of the target may not be matched with the predicted motion of the given tracking model when the vehicles are maneuvered by the drivers. For example, the lateral velocity is considered noise when the state is predicted by an LK model while the vehicle is changing the lane. This can lead to severe prediction error and even loss of tracking. Adding some additional state variables which describe the maneuver in other dimensions may help, such as applying the LC model. However, the system noise may also be introduced when the models with more state variables are considered, which leads to performance
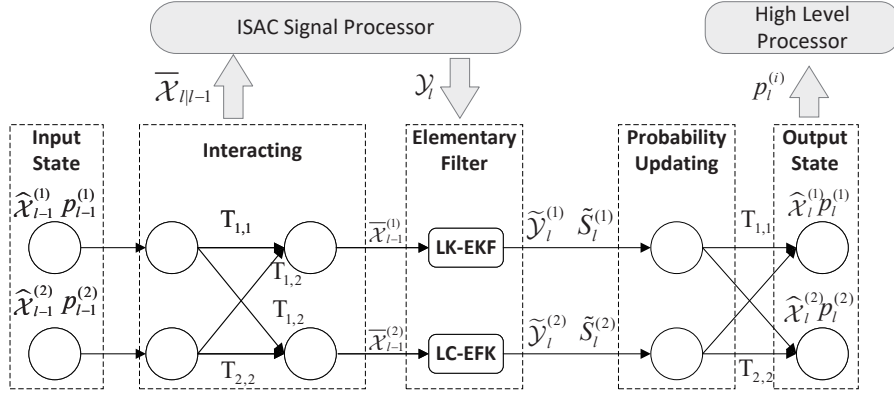
Fig. 4. A flowchart of the IMM filter scheme.

degeneration when the vehicle is stably moving. To improve the robustness of the tracking when maneuver occurs and guarantee the effectiveness when the vehicle is in a stable state, we invoke the IMM filtering algorithm.

An IMM filter scheme is designed for estimating the state of a system that may be matched with more than one potential model (hypothesis). As shown in Fig. 4, an IMM filtering scheme consists of three steps: interacting, elementary filtering, and model probability updating and combining. The estimation and prediction of each model are calculated by a Kalman filter in the second step, and the results of different models interact at the initial and the final step of an IMM filter. Compared with Kalman filters with only one hypothesis, the transition probability matrix $\mathbf{T}$ between different hypotheses is needed as prior information. The entry in the j-th column and the i-th row of $\mathbf{T}$ represents the transition probability from the j-th model to the i-th model, which is irrelative to the estimation but only depends on the kinematic model and road geometry.

In the first step of the IMM filter scheme at the l-th epoch, the probability, estimated state, MSE matrix, and predicted state are regarded as input. We first calculate the mixed probability, which represents the weight of each model at this epoch. By mixing the estimated probability of each model and the transition probability matrix, the mixed probability can be expressed as

$$c_l^{(i|j)} = \left(T_{j,i} p_{l-1}^{(j)} \right) \Big/ \left(\sum_j T_{j,i} p_{l-1}^{(j)} \right), \tag{34}$$

where $p_{l-1}^{(j)}$ is the estimated probability of the j-th model at the $(l$-1$)$-th epoch. Then, the input of the i-th elementary filter can be calculated by mixing the output of all the filters and the mixed probability c as follows

$$\bar{\mathcal{X}}_{l-1}^{(i)} = \sum_j \hat{\mathcal{X}}_{l-1}^{(j)} c_l^{(i|j)}, \quad \bar{\mathcal{X}}_{l|l-1}^{(i)} = \sum_j g^{(i)}(\hat{\mathcal{X}}_{l-1}^{(j)}) c_l^{(i|j)}, \tag{35}$$

$$\bar{\mathbf{M}}_{l-1}^{(i)} = \sum_j c_l^{(i|j)} \times (\mathbf{M}_{l-1}^{(j)} + (\bar{\mathcal{X}}_{l-1}^{(i)} - \hat{\mathcal{X}}_{l-1}^{(j)})(\bar{\mathcal{X}}_{l-1}^{(i)} - \hat{\mathcal{X}}_{l-1}^{(j)})^T). \tag{36}$$

Besides, to construct the transmit beamformer, it is necessary to calculate the mixed prediction for the interacted model by the following equation,

$$\bar{\mathcal{X}}_{l|l-1} = \sum_i \bar{\mathcal{X}}_{l|l-1}^{(i)}/N, \tag{37}$$

where N is the number of hypotheses. [3]

After that, the standard EKFs are employed as elementary filters to respectively estimate and predict the state. Each elementary filter contains six steps, which are listed as below [29]

1) *State Prediction:*

$$\hat{\mathcal{X}}_{l|l-1}^{(i)} = g^{(i)}(\hat{\mathcal{X}}_{l-1}^{(i)}), \tag{38}$$

2) *Linearization:*

$$\mathbf{G}_{l-1}^{(i)} = \frac{\partial g^{(i)}}{\partial \mathcal{X}}\bigg|_{\mathcal{X}=\hat{\mathcal{X}}_{l-1}^{(i)}}, \mathbf{H}_l^{(i)} = \frac{\partial h^{(i)}}{\partial \mathcal{X}}\bigg|_{\mathcal{X}=\hat{\mathcal{X}}_{l|l-1}^{(i)}}, \tag{39}$$

3) *MSE Matrix Prediction:*

$$\mathbf{M}_{l|l-1}^{(i)} = \mathbf{G}_{l-1}^{(i)}\mathbf{M}_{l-1}^{(i)}\mathbf{G}_{l-1}^{(i)H} + \mathbf{Q}_s^{(i)} \tag{40}$$

4) *Residual Covariance and Kalman Gain Calculation:*

$$\mathbf{S}_l^{(i)} = \mathbf{H}_l^{(i)}\mathbf{M}_{l|l-1}^{(i)}\mathbf{H}_l^{(i)H} + \mathbf{Q}_m, \tag{41}$$

$$\mathbf{K}_l^{(i)} = \mathbf{M}_{l|l-1}^{(i)}\mathbf{H}_l^{(i)H}\left(\mathbf{S}_l^{(i)}\right)^{(-1)}, \tag{42}$$

5) *Measurement Residual and State Update:*

$$\tilde{\mathcal{Y}}_l^{(i)} = \mathcal{Y}_l^{(i)} - h^{(i)}(\hat{\mathcal{X}}_{l|l-1}^{(i)}), \quad \hat{\mathcal{X}}_l^{(i)} = \hat{\mathcal{X}}_{l|l-1}^{(i)} + \mathbf{K}_l^{(i)}\tilde{\mathcal{Y}}_l^{(i)} \tag{43}$$

6) *MSE Matrix Update:*

$$\mathbf{M}_l^{(i)} = (\mathbf{I} - \mathbf{K}_l^{(i)}\mathbf{H}_l^{(i)})\mathbf{M}_{l|l-1}^{(i)}, \tag{44}$$

where $i = 1, 2$ denotes the index of models. To be mentioned, the simple EKF can be implemented by removing the model index and employing the steps above.

In the last step, the likelihood L and the probability p for the i-th model at the l-th epoch are updated by analyzing the

---

[3]Although we regard the interacting step as the first step of the IMM filter, we need to calculate all these variables at the end of the previous epoch to output the best prediction of the best beam pattern in this epoch in (5).

measurement residual and the residual covariance matrix by the following equations:

$$L_l^{(i)} = \frac{\exp\left(-\frac{1}{2}\left(\tilde{\mathcal{Y}}_l^{(i)}\right)^T\left(\tilde{\mathbf{S}}_l^{(i)}\right)^{-1}\tilde{\mathcal{Y}}_l^{(i)}\right)}{(\sqrt{(2\pi)^n|\tilde{\mathbf{S}}_l^{(i)}|}}, \qquad (45)$$

$$p_l^{(i)} = \frac{L_l^{(i)}\sum_j T_{j,i}p_{l-1}^{(j)}}{\sum_i\left(L_l^{(i)}\sum_j T_{j,i}p_{l-1}^{(j)}\right)}. \qquad (46)$$

By following the steps above, the fitnesses between the actual states and the hypotheses are measured by probabilities, and the beamformer is almost determined by the model with the best matching probability. Besides, the overall output state and corresponding MSE matrix can be expressed as

$$\hat{\mathcal{X}}_l = \sum_j \hat{\mathcal{X}}_l^{(j)}p_l^{(j)}, \qquad (47)$$

$$\mathbf{M}_l = \sum_j p_l^{(j)}\times(\mathbf{M}_l^{(j)}+(\hat{\mathcal{X}}_l^{(i)}-\hat{\mathcal{X}}_l)(\hat{\mathcal{X}}_l^{(i)}-\hat{\mathcal{X}}_l)^T), \quad (48)$$

which can be employed to analyze the estimation and prediction performances. The overall IMM-EKF scheme is summarized in Algorithm 1 for clarity.

Algorithm 1 IMM-EKF algorithm

Input : Transition probability matrix $\mathbf{T}$, estimated probabilities $p_{l-1}^{(i)}$, estimated states $\hat{\mathcal{X}}_{l-1}^{(i)}$, estimated MSE matrices $\mathbf{M}_{l-1}^{(i)}$, state evolution models $g^{(i)}$, measurement models $h^{(i)}$, covariance matrices $\mathbf{Q}_s^{(i)}$ $\forall i = 1, 2$.

Output Transmit beamformer $\mathbf{f}_l$, estimated probabilities $p_l^{(i)}$, estimated states $\hat{\mathcal{X}}_l^{(i)}$, estimated MSE matrices $\mathbf{M}_l^{(i)}$.

1. Update the mixed probability $c_l^{(i|j)}$, the mixed estimated state $\bar{\mathcal{X}}_l^i$, the mixed predicted elementary state $\bar{\mathcal{X}}_{l|l-1}^i$, the mixed MSE matrix $\bar{\mathbf{M}}_{l-1}^{(i)}$, $(i, j = 1, 2)$, by employing (34), (35), and (36).

2. Update the mixed state $\bar{\mathcal{X}}_{l|l-1}$ and the corresponding beamformer $\mathbf{f}_l$ based on (37) and (5).

3. Obtain the measurements and their corresponding covariance matrix by employing the estimators.

4. Execute the elementary filtering based on (38)-(44).

5. Update the likelihood and the probabilities based on (46).

6. Calculate the output state and the output MSE matrix by employing (48).

IV. DYNAMIC BEAMWIDTH SCHEME FOR ISAC V2I LINK

The transmit beam should be as narrow as possible to achieve high array gain once the accurate location of the vehicle is predicted. However, the accuracy of the IMM-EKF algorithm is limited by both the system noise and measurement noise. This indicates that in the massive-MIMO regime, the vehicle may locate at the sidelobe which accordingly leads to low array gain and poor sensing and communication performance. In this section, we propose a dynamic beamwidth method to provide robust array gain with given misalignment probability by analyzing the uncertainty of the prediction.

A. Analysis on Prediction Uncertainty and Array Gain

To characterize the uncertainty of the prediction, we derive the distribution of the predicted state, which has a direct impact on beamforming. Following the definition of the MSE matrix in the EKF algorithm, the expectation of error between the predicted state and the true state can be given as

$$\mathbb{E}\{(\hat{\mathcal{X}}_{l|l-1}-\mathcal{X}_l)(\hat{\mathcal{X}}_{l|l-1}-\mathcal{X}_l)^H\}$$
$$=\mathbb{E}\{(g(\hat{\mathcal{X}}_{l-1})-g(\mathcal{X}_{l-1})-\boldsymbol{\omega}_l)(g(\hat{\mathcal{X}}_{l-1})-g(\mathcal{X}_{l-1})-\boldsymbol{\omega}_l)^H\}$$
$$\overset{(a)}{\approx}\mathbb{E}\{\left(\mathbf{G}_{l-1}(\hat{\mathcal{X}}_{l-1}-\mathcal{X}_{l-1})-\boldsymbol{\omega}_l\right)\left(\mathbf{G}_{l-1}(\hat{\mathcal{X}}_{l-1}-\mathcal{X}_{l-1})-\boldsymbol{\omega}_l\right)^H\}$$
$$\overset{(b)}{=}\mathbf{G}_{l-1}\mathbf{M}_{l-1}\mathbf{G}_{l-1}^H+\mathbf{Q}_s=\mathbf{M}_{l|l-1}, \qquad (49)$$

where the linear approximation (a) follows by the linearization step of EKF and (b) follows by the fact that the system noise $\boldsymbol{\omega}_l$ is independent to $\mathcal{X}_{l-1}$ and $\hat{\mathcal{X}}_{l-1}$, i.e., $\mathbb{E}\{\mathcal{X}_{l-1}\boldsymbol{\omega}_l^H\}=0$ and $\mathbb{E}\{\hat{\mathcal{X}}_{l-1}\boldsymbol{\omega}_l^H\}=0$. Since both $\hat{\mathcal{X}}_{l-1}$ and $\boldsymbol{\omega}_l$ are Gaussian distributed, $\hat{\mathcal{X}}_{l|l-1}$ is Gaussian distributed as well, which subject to $\hat{\mathcal{X}}_{l|l-1}\sim\mathcal{CN}(\mathcal{X}_l,\mathbf{M}_{l|l-1})$.

As our main purpose is to find the proper beamwidth, we focus on the state variables s and n, which are relative to φ and θ. The uncertainty of the angle can be modeled as

$$\Psi = \begin{bmatrix}\Delta\theta_l\\\Delta\varphi_l\end{bmatrix}=\begin{bmatrix}\hat{\theta}_{l|l-1}-\theta_l\\\hat{\varphi}_{l|l-1}-\varphi_l\end{bmatrix}\approx\begin{bmatrix}\frac{\partial\theta}{\partial s}&\frac{\partial\theta}{\partial n}\\\frac{\partial\varphi}{\partial s}&\frac{\partial\varphi}{\partial n}\end{bmatrix}\begin{bmatrix}\hat{s}_{l|l-1}-s_l\\\hat{n}_{l|l-1}-n_l\end{bmatrix}, \qquad (50)$$

where we apply the first-order linear approximation in the above equation due to the non-linearity between the angle and the state variables. With the distribution of predicted state $\hat{\mathcal{X}}_{l|l-1}$ in hand, one can directly express the distribution of Ψ as

$$\Psi\sim\mathcal{N}(0,\Sigma), \quad \Sigma=\begin{bmatrix}\frac{\partial\theta}{\partial s}&\frac{\partial\theta}{\partial n}\\\frac{\partial\varphi}{\partial s}&\frac{\partial\varphi}{\partial n}\end{bmatrix}\mathbf{M}_{l|l-1}\begin{bmatrix}\frac{\partial\theta}{\partial s}&\frac{\partial\theta}{\partial n}\\\frac{\partial\varphi}{\partial s}&\frac{\partial\varphi}{\partial n}\end{bmatrix}^T. \quad (51)$$

Then, the array gain at the l-th epoch with the beamformer designed to point at $\hat{\theta}_{l|l-1}$ and $\hat{\varphi}_{l|l-1}$ can be expressed as (52). To further reveal the relationship between the array gain and the prediction uncertainty, (52) can be approximated as

$$\kappa^2\approx\Big|\sum_{n=0}^{N-1}\sum_{m=0}^{M-1}e^{j\pi(n\Psi_\parallel+m\Psi_\perp)}\Big|^2$$
$$=MN\frac{\sin^2(\frac{\pi N\Psi_\parallel}{2})}{\sin^2(\frac{\pi\Psi_\parallel}{2}))}\frac{\sin^2(\frac{\pi M\Psi_\perp}{2})}{\sin^2(\frac{\pi\Psi_\perp}{2})}, \qquad (53)$$

with

$$\begin{bmatrix}\Psi_\parallel\\\Psi_\perp\end{bmatrix}=\begin{bmatrix}-\sin\theta\sin\varphi&\cos\theta\cos\varphi\\\sin\theta\cos\varphi&\cos\theta\sin\varphi\end{bmatrix}\begin{bmatrix}\Delta\theta\\\Delta\varphi\end{bmatrix}=\mathbf{T}_\Sigma\Psi. \quad (54)$$

By denoting $\tilde{\Psi}=[\Psi_\parallel,\Psi_\perp]^T$, the distribution and the corresponding PDF can be expressed as

$$\tilde{\Psi}\sim\mathcal{N}(0,\tilde{\Sigma}), f(\tilde{\Psi})=\frac{1}{2\pi|\tilde{\Sigma}|^{\frac{1}{2}}}e^{-\frac{1}{2}\tilde{\Psi}\tilde{\Sigma}^{-1}\tilde{\Psi}^T}, \qquad (55)$$

where $\tilde{\Sigma}=\mathbf{T}_\Sigma\Sigma\mathbf{T}_\Sigma^T$ denotes the covariance matrix.

$$\kappa(\theta_l, \varphi_l, \hat{\theta}_{l|l-1}, \hat{\varphi}_{l|l-1}) = \tag{52}$$
$$\left| \sum_{n=0}^{N-1} \sum_{m=0}^{M-1} \exp\{j\pi\Big(n(\cos\theta_l \sin\varphi_l - \cos\hat{\theta}_{l|l-1}\sin\hat{\varphi}_{l|l-1}) + m(\sin\theta_l \sin\varphi_l - \sin\hat{\theta}_{l|l-1}\sin\hat{\varphi}_{l|l-1}))\}\right|,$$

B. Proposed Beamwidth Control Method

Due to the limitation of prediction precision, the beam should be properly widened. Thus, our goal is to find a minimal beamwidth and the corresponding minimal beam-covered area D_0 to provide high array gain while guaranteeing the misaligned probability lower than a given threshold Γ. This task can be mathematically formulated as

$$\begin{aligned} \min \quad & D_0 \\ s.t. \quad & \iint_{D_0} f(\tilde{\Psi})dD > 1 - \Gamma. \end{aligned} \tag{56}$$

With the given threshold, one may employ a two-dimensional linear search to find the optimal beamwidth, which could be computationally expensive. On this basis, we propose a dynamic beamwidth method, which calculates the sub-optimal solution in closed form.
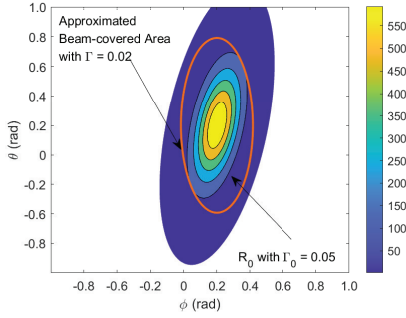

Fig. 5. Contour plot of $f(\tilde{\Psi})$, best area with Γ_0 and the approximated beam-covered area.

Since the double integral on the θ-φ plane, which integrates the PDF grid-by-grid, is difficult to solve, we resort to calculating the integral circle-by-circle from the center point. By defining the radius scale r as $r^2 = \tilde{\Psi}^H \tilde{\Sigma}^{-1} \tilde{\Psi}$, the cumulative probability in the area D_1 where $r < R_0$ can be expressed as

$$\begin{aligned} F(R_0) &= \iint_{D_1(R_0)} f(\tilde{\Psi})dD = \int_0^{R_0} \frac{1}{2\pi|\tilde{\Sigma}|^{\frac{1}{2}}} e^{-\frac{1}{2}r^2} 2\pi|\tilde{\Sigma}|^{\frac{1}{2}} r dr \\ &= 1 - e^{-\frac{1}{2}R_0^2}. \end{aligned} \tag{57}$$

Accordingly, as shown in Fig. 5, for any given Γ_0, it is possible to find a corresponding R_0 which guarantees the cumulative probability being equal to $1 - \Gamma_0$.

Since $\tilde{\Sigma}$ is not a diagonal matrix, the area D_1 is a rotated eclipse while the beam-covered area is a set of standard eclipses. This makes it difficult to find the optimal beam-covered area by directly employing R_0. Therefore, as shown in Fig. 5, we turn to find the sub-optimal region $\tilde{D}_0 \supseteq D_1(R_0)$ where the misalignment probability is less than Γ which results

in little performance loss. By simple geometric derivation, the expression of the sub-optimal beam-covered area which covers $D_1(R_0)$ with the highest array gain can be given as

$$\tilde{D}_0 : A_\theta \theta^2 + B_\varphi \varphi^2 \leq 1. \tag{58}$$

In the above equation, A_θ and B_φ are the parameters of the semi-major axis and semi-minor axis of $\tilde{D}_0$, which can be expressed as

$$A_\theta = \tilde{\Sigma}_{1,1}^{-1} - |\tilde{\Sigma}_{2,1}^{-1}|\sqrt{\tilde{\Sigma}_{1,1}^{-1}/\tilde{\Sigma}_{2,2}^{-1}}/2, \tag{59a}$$

$$B_\varphi = \tilde{\Sigma}_{2,2}^{-1} - |\tilde{\Sigma}_{1,2}^{-1}|\sqrt{\tilde{\Sigma}_{2,2}^{-1}/\tilde{\Sigma}_{1,1}^{-1}}/2, \tag{59b}$$

with $\tilde{\Sigma}_{i,j}^{-1}$ being the element in i-th column and j-th row of the inversed covariance matrix. Further, the corresponding beamwidth can be expressed as $\theta_{BW} = \sqrt{1/A_\theta}$ and $\varphi_{BW} = \sqrt{1/B_\varphi}$.

In the mMIMO regime, the beamwidth is almost continuous to the number of stimulated antennas. Therefore, for ease of implementation, we employ a rectangular window to control the beamwidth, where the number of the non-zero elements are denoted as $\tilde{M}$ and $\tilde{N}$ in the two directions. By employing separable spectral weightings method, the optimal $\tilde{M}$ and $\tilde{N}$ can be directly given as [30]

$$\tilde{N}^* = \left\lfloor 0.89 \sqrt{\frac{\tilde{\Sigma}_{2,1}\sqrt{\tilde{\Sigma}_{1,1}}}{8\sqrt{\tilde{\Sigma}_{2,2}}}} \right\rfloor, \tilde{M}^* = \left\lfloor 0.89 \sqrt{\frac{\tilde{\Sigma}_{2,1}\sqrt{\tilde{\Sigma}_{2,2}}}{8\sqrt{\tilde{\Sigma}_{1,1}}}} \right\rfloor. \tag{60}$$

The overall algorithm is summarized in Algorithm 2.

Algorithm 2 Dynamic Beamwidth control scheme

Input : Desired misalignment probability Γ, predicted State $\hat{\mathcal{X}}_{l|l-1}$, predicted MSE matrix $\hat{M}_{l|l-1}$, Jacobian matrix for evolution function G_{l-1}.

Output The number of the non-zero elements of the rectangular window $\tilde{M}^*$ and $\tilde{N}^*$.

1. Calculate the covariance matrix by using (51) and (55).
2. Get the radius scale factor R_0 by calculating $F(R_0) < 1 - \Gamma$ in (57).
3. Normalize the covariance matrix and calculate the corresponding sub-optimal beam-covered area by using (58).
4. Calculate the sub-optimal beamwidth in (59) and control the beamwidth by employing (60).

V. NUMERICAL RESULTS

In this section, we evaluate the performance of our proposed scheme in both sensing and communication functionalities by using numerical simulation. Unless otherwise specified, both the RSU and the vehicle operate at $f_c = 30\text{GHz}$ with
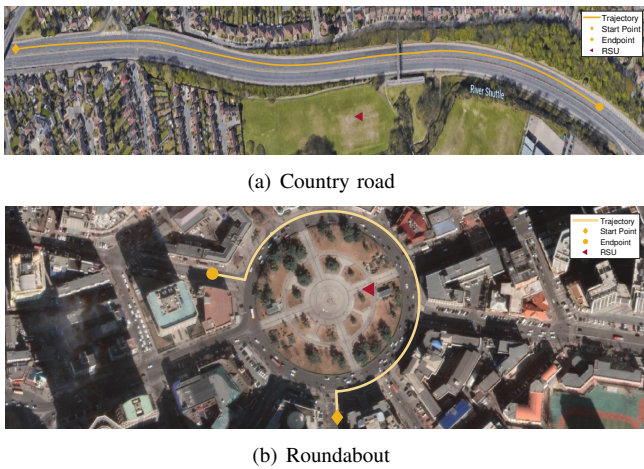
(a) Country road

(b) Roundabout

Fig. 6. Two road models used in the simulation.

a bandwidth B_w as 500MHz, the transmit power P_t is considered as $P_t = 30$dBm, and the data-frame block duration is set as $\Delta T = 20$ms. The noise power spectral density is considered as -144 dBm/Hz at all the receivers, which leads to the variance of the noise as -57 dBm. The path losses for both sensing and communication functions are calculated by applying the free space transformation model. The road models applied in this section are imported from Google Earth and shown in Fig. 6. We choose the center line of the roads as the s axes of the CCSs and regard them as the ideal trajectories. We choose 50 control points in Fig. 6(a) and 30 control points in Fig. 6(b) with considering the curvature and the shape of the roads. The first model is a part of the country road in London, UK, with longitude and latitude coordinates being 51°26'52"N, 0°08'54"E. In this model, the coverage of the RSU is assumed to be 200m and the minimum distance from the road to the RSU is 15m. The second model is a roundabout in Dalian, China, with coordinates being 38°55'14"N, 121°37',20"E. The radius of the roundabout is 50m, which follows existing standards in China with the maximum velocity of the vehicle being limited to 10m/s [31], and with the origin of the Cartesian coordinate system is set as the center of the roundabout. The RSU is located at $\{18, 15\}$ in the Cartesian system in order to sense the Doppler shift along the road. The variances of system noise for both models are set as follows: $\sigma_s = 0.08$m, $\sigma_n = 0.016$m, $\sigma_{v_s} = 0.1$m/s, $\sigma_{v_n} = 0.02$m/s, $\sigma_\beta = 2 \times 10^{-6}$, and the covariance matrix of the measurement noise is calculated in EKF procedure by applying (24) and (26-27). Moreover, to separately explore the improvement of each proposed scheme, the dynamic beamwidth scheme is only applied in the last subsection.

A. Performance for Tracking the Vehicle in the LK Model

We first evaluate the communication and sensing performances of the proposed technique under the LK assumption. Without loss of generality, we set the initial state of the vehicle as $s = 2$m, $v_s = 10$m/s, $n = 0$m, $\beta = 2 \times 10^{-5} \times (1 + j)$.

In Fig. 7, we show the downlink achievable rates of the communication link with the increased size of the antenna
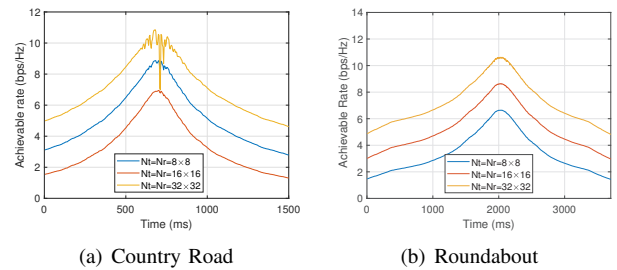

(a) Country Road

(b) Roundabout

Fig. 7. Achievable rate for proposed scheme, with initial state $s = 2$m, $v_s = 10$m/s, $n = 0$m, $\beta = 2 \times 10^{-5} \times (1 + j)$, $P_t = 30$dBm.

(a) RMSE of the longitudinal distance in the country road.

(b) RMSE of the longitudinal distance in the roundabout.

(c) RMSE of the lateral distance in the country road.
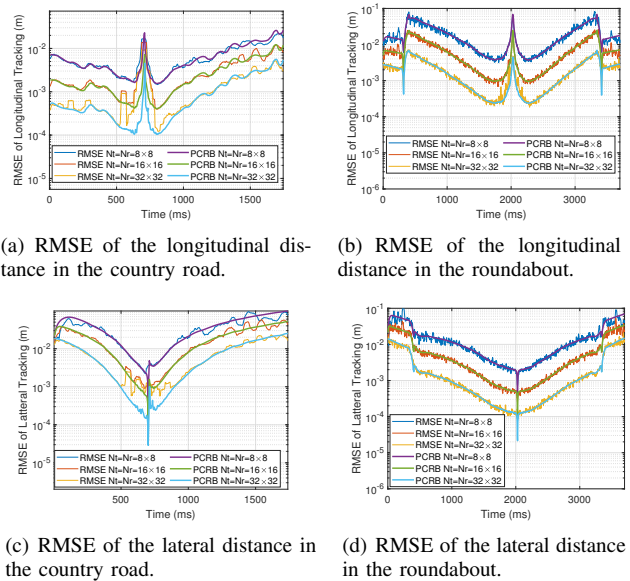

(d) RMSE of the lateral distance in the roundabout.

Fig. 8. Position tracking performance for proposed scheme , with initial state $s = 2$m, $v_s = 10$m/s, $n = 0$m, $\beta = 2 \times 10^{-5} \times (1 + j)$, $P_t = 30$dBm.

array. In both scenarios, the initial location of the vehicle is far from the RSU, which leads to low SNRs and corresponding low achievable rates. When the vehicle is approaching the RSU, the path-losses decrease with respect to the distance, which accordingly leads to increasing achievable rates. Note that, the communication performance degenerates when the vehicle is quite near to the RSU in the country road model when $N_t = 32 \times 32$. On the one hand, the velocity of the vehicle is almost vertical to the propagation direction of the signal, which makes the Doppler frequency hard to be estimated. On the other hand, since the distance between the RSU and the vehicle is sufficiently small, the angle changes too fast for EKF tracking. Fortunately, this degeneration does not occur when the size of the antenna array is small and can also be compensated by the dynamic beamforming algorithm proposed in Sec. IV when the size of the antenna array is large.

In Fig. 8, we demonstrate the radar sensing performance in terms of root mean squared error (RMSE) for the position tracking performance in the CCS and reveal how the communication performance depends on the sensing performance. As shown in Fig. 8, benefiting from the improvement of the SNR and the accuracy of the measurement in each epoch, the tracking performances generally increase when the vehicle is
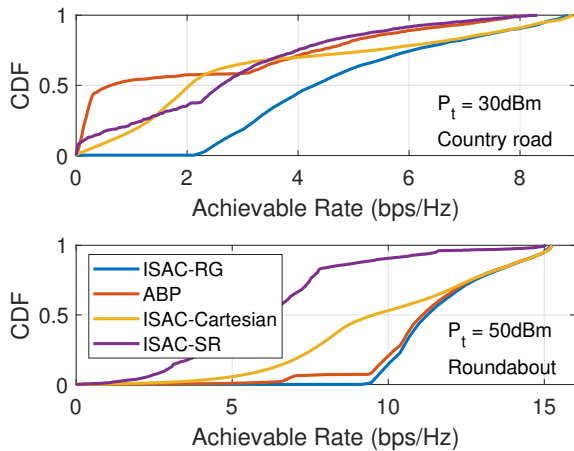
Fig. 9. CDF of achievable rates for different algorithms with $N_t = N_r = 256$, $P_t = 30$dBm and 50dBm.

Fig. 10. Achievable rates comparison for different algorithms with $N_t = N_r = 256$, $P_t = 30$dBm and 50dBm.

moving near the RSU. Moreover, when the direction of the vehicle is almost perpendicular to the RSU (700ms in (a) and (c), and 2100ms in (b) and (d)), it is difficult to track the Doppler shift in the longitudinal direction while the tracking performance in the lateral direction is improved. The spikes in the RMSEs in (b) and (d) (at about 500ms and 3500ms) are due to the swift direction changes when entering and exiting the roundabout in Fig. 6(b). When the vehicle is near enough to the RSU, the angle prediction error is sensitive to the location prediction error. Such that, the large error of longitudinal distance prediction error in the country road model leads to slight beam alignment and corresponding communication performance degeneration in Fig. 7(a). It is noteworthy that, when the beam precisely points to the vehicle, the RMSE is tightly bounded by PCRB, which proves the effectiveness of the proposed scheme in Sec. IV that dynamically adjusts the beamwidth by leveraging the predicted MSE matrix.

B. Performace Comparision for Proposed Algorithm and Benchmark Schemes

In this subsection, we examine the superiorities of our proposed algorithm (ISAC-RG) by comparing it with the following beam tracking schemes in the country road model:

- The ISAC-based beam tracking scheme in the Cartesian coordinate system, which predicts the state of the vehicle on the complicated road by applying a difference algorithm (ISAC-Cartesian). [14].
- The ISAC-based beam tracking scheme which assumes the vehicles are driven on a straight road (ISAC-SR). [11].
- The auxiliary beam pair algorithm where quaternary training beams are transmitted to the vehicle at the beginning of an epoch (ABP) [20].

Note that the ABP algorithm is a kind of communication-only beam tracking algorithm that needs additional uplink feedback to inform the RSU of the channel estimation, thus the overhead is much higher than that of ISAC-based algorithms. The ISAC-Cartesian algorithm is applied to situations where the state evolution functions are difficult to derive and usually has some
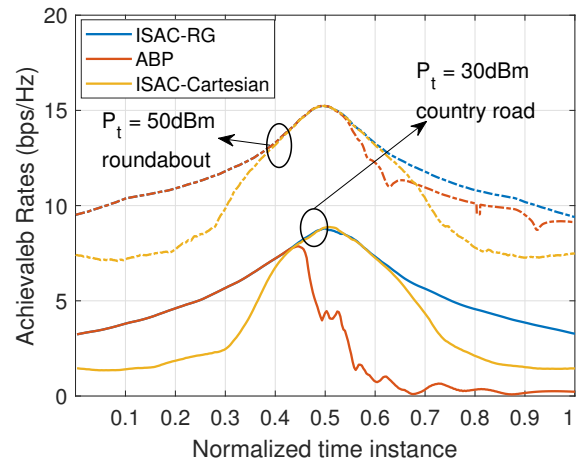
performance loss. Here, the number of transmit and receive antennas is assumed to be 256, and the half-searching range of both elevation and azimuth beamforming region for the ABP algorithm is set as $\pi/8$ without loss of generality.

In Fig. 9, we first explore the communication performance by showing the empirical cumulative distribution functions (CDF) in terms of the achievable rates. It is notable to see that the proposed algorithm always achieves the best performance compared with the benchmark schemes and shows robustness to the transmit power budget. It can also be seen that the gap in communication performance between the ISAC-Cartesian and the proposed algorithm reduces as the transmit power increases, and the gap between the ABP and the ISAC-RG also decreases since the roundabout model is friendly to the ABP algorithm. As for the ISAC-SR, the mismatched model makes it difficult to track the vehicle properly and leads to severe performance loss.

We further show the achievable rates obtained for different schemes in one realization in Fig. 10 to interpret how the movement of the vehicle affect communication performance. To be mentioned, we do not show the ISAC-SR in this figure since the reason for performance loss is obvious and the performance with a higher power budget has too many crossovers with that of other schemes with a lower budget. It can be seen that the ABP algorithm shows comparable performance when the vehicle is moving to the RSU (0 to 0.5), and suffers severe performance loss after passing the RSU. This is because the ABP algorithm exploits the feedback direction information to perform beam tracking, whose performance relies on the accuracy of angle estimation in the current epoch but not all the past epochs, which results in instability of tracking. More specifically, once the angle begins to vary rapidly, the beam misalignment may become severe. As a result, an outage may occur in tracking and communication with the VU. Moreover, because the minimum distance from the vehicle to the RSU in the roundabout is much larger than that in the country road, the angular velocity is smaller and leads to fewer performance losses. As for the
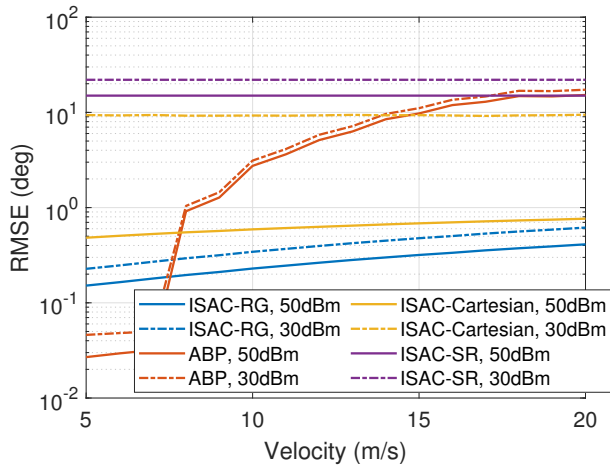
Fig. 11. RMSE of the angle prediction versus the velocity of the vehicle in the country road model.
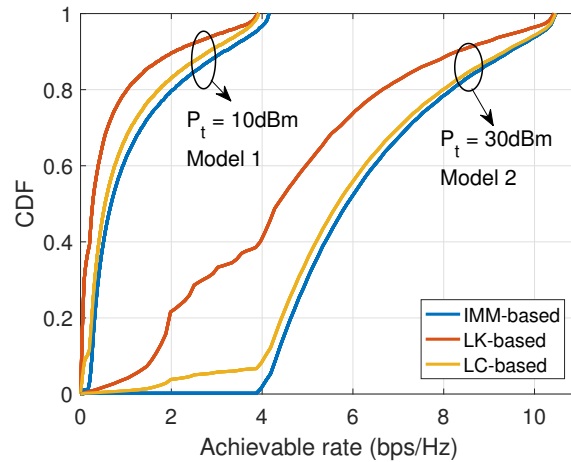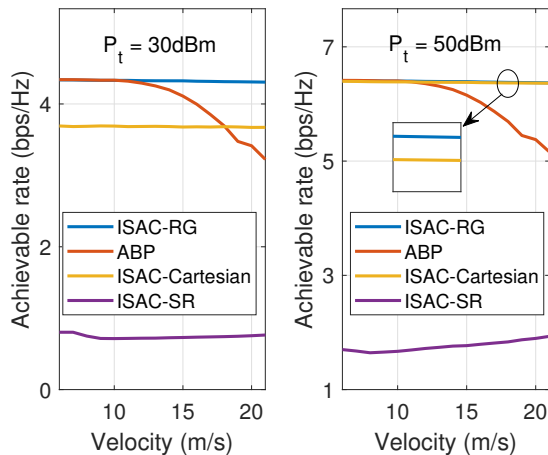

Fig. 12. Average achievable rate versus the velocity of the vehicle in the country road model.

ISAC-Cartesian algorithm, since the prediction performance only relies on the measurement in the last three steps and the RMSE of the prediction is several times of the RMSE of the estimation, the achievable rate is more relevant to radar SNR compared with the proposed algorithm. As shown in the figure, the performance is comparable with the proposed algorithm in the area near the RSU where the radar SNR is high enough, but severe performance degenerations occur in the other area.

To verify the superiority of the proposed method in high-mobility scenarios and to further discuss the impact of the sensing performance on the communication performance, we show the overall RMSE result of the angle prediction and the average achievable rate versus velocity in Fig. 11 and Fig. 12. In general, the performance of the ISAC-RG and ISAC-Cartesian is robust to the change of the velocity, while the performance of the ABP algorithm degenerates quickly when the velocity is high. As we mentioned above, the accuracy of the proposed EKF-based algorithm mainly relies on estimation accuracy in all past observations and the system noise, which is more reliable in high-mobility networks. For the ABP algorithm, the uncertainty imposed by the prediction

Fig. 13. CDF of achievable rates for the IMM-based algorithm and single-model-based algorithms in the maneuver scenarios.

is avoided by using the feedback information, which leads to better performance in the low-velocity regime. However, when the angular variation becomes large, the ABP method quickly breaks down. Meanwhile, since the ISAC-SR adopts a mismatched state evolution model, it is not able to track the vehicle properly and the communication performance mainly relies on the power budget. It is also obvious that the communication performance is generally dominated by the sensing performance with a given power budget. For example, the RMSE of the ABP algorithm increases when the velocity is larger than 8m/s while the communication performance also degenerates in the same region. It is noteworthy that, the improvement of the achievable rate is negligible when the RMSE is low enough since the array gain is almost flat in the center of the main lobe.

C. Performance for IMM tracking and Behavior Reasoning

In this part, we study the performance of the proposed IMM-based tracking scheme. We consider two scenarios where the vehicle tries to maneuver at a constant lateral velocity on the country road. In the first scenario, the vehicle firstly moves stably at a longitudinal velocity of 5m/s from 0ms to 600ms. Then the vehicle changes its lane from 600ms to 1200ms at a lateral velocity of 1m/s while the longitudinal velocity is still 5m/s. After that, the vehicle continues to move stably. In the second scenario, the vehicle has the same state as the first scenario before 1200ms but quickly changes its lane to the other direction in 2m/s from 1200ms to 2000ms. The lateral velocity in the two scenarios is demonstrated as the bottom bar in Fig. 14.

In Fig. 13, we investigate the comparison of communication performance between the IMM-based algorithm and the single-model-based algorithms by showing the CDF versus achievable rates. It is obvious that the IMM-based shows superiority over the single-model-based algorithms in the given scenarios. More specifically, the achievable rate of the LK-based algorithm always has a notable gap between the other schemes which verifies that the EKF with the LK model
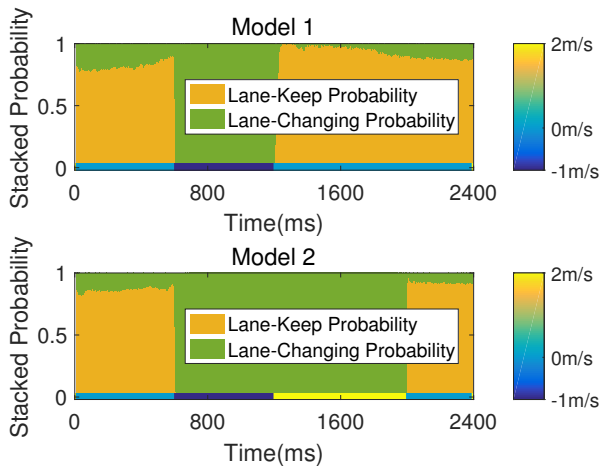
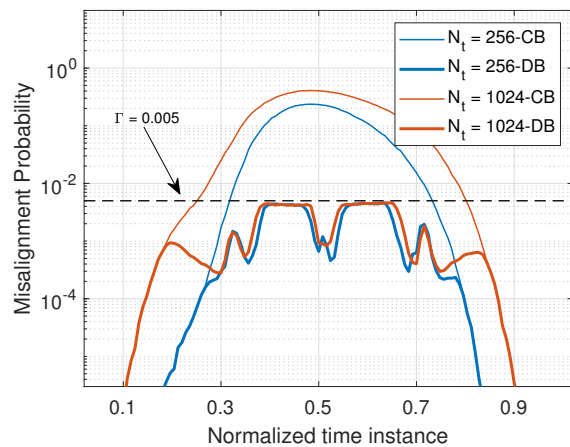Fig. 14. Reasoning Performance of IMM-based algorithm.

Fig. 15. Misalignment probability of constant beamwidth scheme and proposed dynamic beamwidth scheme when the vehicle is near to the RSU in country road model.
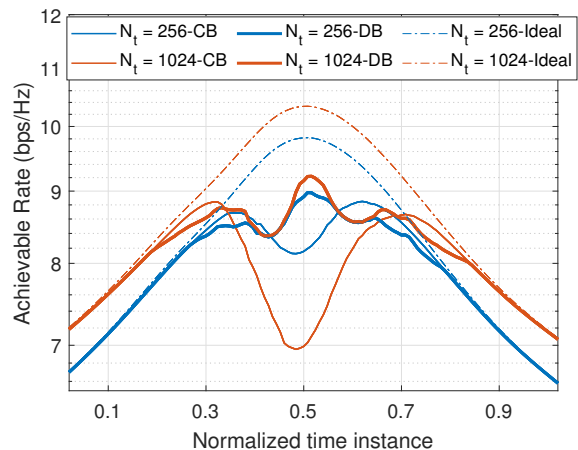

Fig. 16. Achievable rate of constant beamwidth scheme and proposed dynamic beamwidth scheme when the vehicle is near to the RSU in country road model.

is difficult to generalize to other models. The performance of the LC model also lags behind the IMM-based algorithm, especially in scenario 1 in which the vehicle only slightly changes lanes. It is because the LC model introduces an additional state variable to track the lateral movement and leads to more system noise and larger error of angle prediction, even though the vehicle is moving stably.

Then we show the stacked probability of the two models in Fig. 14 to evaluate the reasoning ability of the IMM-based algorithm. As shown in both the subfigures, when the lateral velocity is not zero, the probability of the LC model is close to 1, which indicates that we can always identify the lane-changing operation. In the other situations, the probability of the LK model is not always close to 1 which slightly impairs the tracking performance. However, the reasoning performance is still guaranteed since the LK probability is larger than 0.5, which is usually regarded as a threshold of identification. [4]

D. Performance for Dynamic Beamforming

In this subsection, we compare the misalignment probability and achievable rate between the general constant beamwidth (CB) algorithm which tries to form the narrowest beam and our proposed dynamic beamwidth (DB) scheme which guarantees a given misalignment probability. To be mentioned, we assume the system noise as $\sigma_s = 0.16m$ and $\sigma_n = 0.0032m$ to reveal the performance under a worse situation where the error of the roadway geometry map is larger or the behavior of the vehicle is more unpredictable.

In Fig. 15, we first evaluate the misalignment probability of the two schemes. It can be observed that the misalignment probability of the CB algorithm increases with respect to the size of the antenna array while that of the DB algorithm is always lower than the given threshold. Then we focus on the tendency of probability to change along the positional

[4]Note: It is worth mentioning that we assume the lateral velocity is a constant when the vehicle changes its lane and mutated when the changing is stopped. This is an extreme case that barely occurs on the real-world road but can prove that the proposed algorithm is able to work even in extreme cases.

axis. The change of the CB algorithm is obviously intuitive, where the misalignment probability increases with the vehicle nearing the RSU. It is worth pointing out that there is a distinct gap between the threshold and the actual misalignment probability of the DB scheme at some certain points. The first reason for this phenomenon is that when the size of the antenna is small, the discreteness of adjustment makes it impossible to achieve the best beam-covered area and accordingly leads to lower misalignment probability and potential performance loss of achievable rate. The second reason is that when the cross-correlation between the two spatial frequencies is large, the rotation angle of the eclipse of the PDF is approximated to be $\pi/4$ while that of the beam-covered area is always 0, which results in the largest residual error of the approximation.

We then compare achievable rates of the proposed scheme, the CB scheme and the ideal scenario where the system always has a full array gain in Fig.16. Both the algorithms show the same performance with the ideal scenario when the vehicle is far from the RSU where the misalignment probability is low enough which is consistent with the analysis above. As the

misalignment of DB algorithm is lower, the communication performance shows superiority over the DB algorithm and inferiority as compared with the ideal scenario. In addition, it is interesting to note that crossover occurs in the area where the performance curves begin to separate, which is because the discreteness of the array size and the residual error leads to excessive adjustment and performance loss. Fortunately, the degeneration is moderate and may not occurs in other circumstance.

TABLE I
COMPUTATIONAL COMPLEXITY FOR DIFFERENT ALGORITHMS PER DATA FRAME.

	ISAC-RG	ISAC-Cartesian	ABP	ISAC-SR
Analytical	$\mathcal{O}(K\zeta)$	$\mathcal{O}(K)$	$\mathcal{O}(K)$	$\mathcal{O}(K)$
Numerical (μs)	53.29	8.25	4.73	21.73

To verify the practical feasibility of introducing the IMM-EKF-based algorithm with dynamic beamwidth adjustment under the CCS, we give a brief discussion on the complexity of our proposed method. The number of the VU K is assumed to be 1 and the number of the potential kinematic ζ is assumed to be 2 in this simulation. The simulation is performed on an Intel Core i5-11500T CPU 32GB RAM computer with 1.5GHz. As shown in Table 1, the overheads of the benchmarks are all $\mathcal{O}(K)$ while that of the proposed method is $\mathcal{O}(K\zeta)$. The additional overhead comes from the IMM algorithm which simultaneously tracks multiple kinematic models. However, since there is no iterative procedure in the proposed method (neither in the benchmarks), the average per-frame execution time on the PC is 53.29 μs, which can be greatly reduced on a 5G cellular base station. Moreover, the computing tasks for the elementary filters are irrelative to each other, which means while complexity is $\mathcal{O}(K\zeta)$, the execution time can be reduced to $\mathcal{O}(K)$ by employing parallel computing techniques.

VI. CONCLUSION

In this article, we have proposed a novel predictive beamforming scheme for tracking and communicating with a vehicle on arbitrarily shaped roads by employing an RSU equipped with the ISAC capability. By applying the CCS, the proposed approach enabled the implementation of high-accuracy EKF beam prediction to detect and track the vehicle given any roadway geometries. Furthermore, we have proposed an IMM-based filtering scheme to track and identify vehicle maneuvering. Considering the beam misalignment incurred by system noise and measurement noise, a dynamic beamwidth adjustment algorithm has been further proposed by analyzing the properties of the spatial frequency uncertainty. The algorithm is aimed at maximizing the array gain while ensuring that the misalignment probability is lower than a given threshold. Finally, to validate the effectiveness of our proposed algorithms, numerical results have been provided to show that the IMM-EKF-based predictive beamforming scheme outperforms conventional benchmark techniques. The ability of tracking and identifying the vehicle maneuvering has also been verified. Additionally, the trade-off between the misalignment probability and the array gain has been demonstrated by adopting the dynamic beamwidth scheme.

REFERENCES

[1] H. Wymeersch, G. Seco-Granados, G. Destino, D. Dardari, and F. Tufvesson, "5G mmwave positioning for vehicular networks," *IEEE Wireless Communications*, vol. 24, no. 6, pp. 80–86, 2017.

[2] S. Kuutti, S. Fallah, K. Katsaros, M. Dianati, F. Mccullough, and A. Mouzakitis, "A survey of the state-of-the-art localization techniques and their potentials for autonomous vehicle applications," *IEEE Internet of Things Journal*, vol. 5, no. 2, pp. 829–846, 2018.

[3] J. B. Kenney, "Dedicated short-range communications (DSRC) standards in the united states," *Proceedings of the IEEE*, vol. 99, no. 7, pp. 1162–1182, 2011.

[4] N. Alam, A. T. Balaei, and A. G. Dempster, "An instantaneous lane-level positioning using dsrc carrier frequency offset," *IEEE Transactions on Intelligent Transportation Systems*, vol. 13, no. 4, pp. 1566–1575, 2012.

[5] S. Gyawali, S. Xu, Y. Qian, and R. Q. Hu, "Challenges and solutions for cellular based V2X communications," *IEEE Communications Surveys & Tutorials*, 2020.

[6] M. Gonzalez-Martín, M. Sepulcre, R. Molina-Masegosa, and J. Gozalvez, "Analytical models of the performance of C-V2X mode 4 vehicular communications," *IEEE Transactions on Vehicular Technology*, vol. 68, no. 2, pp. 1155–1166, 2018.

[7] T. S. Rappaport, S. Sun, R. Mayzus, H. Zhao, Y. Azar, K. Wang, G. N. Wong, J. K. Schulz, M. Samimi, and F. Gutierrez, "Millimeter wave mobile communications for 5G cellular: It will work!" *IEEE Access*, vol. 1, pp. 335–349, 2013.

[8] R. W. Heath, N. Gonzalez-Prelcic, S. Rangan, W. Roh, and A. M. Sayeed, "An overview of signal processing techniques for millimeter wave MIMO systems," *IEEE Journal of Selected Topics in Signal Processing*, vol. 10, no. 3, pp. 436–453, 2016.

[9] H. Q. Ngo, *Massive MIMO: Fundamentals and system designs.* Linköping University Electronic Press, 2015, vol. 1642.

[10] N. González-Prelcic, R. Méndez-Rial, and R. W. Heath, "Radar aided beam alignment in mmWave V2I communications supporting antenna diversity," in *2016 Information Theory and Applications Workshop (ITA)*. IEEE, 2016, pp. 1–7.

[11] F. Liu, W. Yuan, C. Masouros, and J. Yuan, "Radar-assisted predictive beamforming for vehicular links: Communication served by sensing," *IEEE Transactions on Wireless Communications*, vol. 19, no. 11, pp. 7704–7719, 2020.

[12] Z. Du, F. Liu, W. Yuan, C. Masouros, Z. Zhang, and G. Caire, "Integrated sensing and communications for V2I networks: Dynamic predictive beamforming for extended vehicle targets," *arXiv preprint arXiv:2111.10152*, 2021.

[13] W. Yuan, F. Liu, C. Masouros, J. Yuan, D. W. K. Ng, and N. González-Prelcic, "Bayesian predictive beamforming for vehicular networks: A low-overhead joint radar-communication approach," *IEEE Transactions on Wireless Communications*, vol. 20, no. 3, pp. 1442–1456, 2020.

[14] F. Liu and C. Masouros, "A tutorial on joint radar and communication transmission for vehicular networks-part III: Predictive beamforming without state models," *IEEE Communications Letters*, 2020.

[15] F. Liu, Y. Cui, C. Masouros, J. Xu, T. X. Han, Y. C. Eldar, and S. Buzzi, "Integrated sensing and communications: Toward dual-functional wireless networks for 6g and beyond," *IEEE Journal on Selected Areas in Communications*, vol. 40, no. 6, pp. 1728–1767, 2022.

[16] D. Zhu, J. Choi, Q. Cheng, W. Xiao, and R. W. Heath, "High-resolution angle tracking for mobile wideband millimeter-wave systems with antenna array calibration," *IEEE Transactions on Wireless Communications*, vol. 17, no. 11, pp. 7173–7189, 2018.

[17] F. Liu, P. Zhao, and Z. Wang, "EKF-based beam tracking for mmWave MIMO systems," *IEEE Communications Letters*, vol. 23, no. 12, pp. 2390–2393, 2019.

[18] J. Lim, H.-M. Park, and D. Hong, "Beam tracking under highly nonlinear mobile millimeter-wave channel," *IEEE Communications Letters*, vol. 23, no. 3, pp. 450–453, 2019.

[19] J. Tan and L. Dai, "Wideband beam tracking in THz massive MIMO systems," *IEEE Journal on Selected Areas in Communications*, vol. 39, no. 6, pp. 1693–1710, 2021.

[20] D. Zhu, J. Choi, and R. W. Heath, "Auxiliary beam pair enabled AoD and AoA estimation in closed-loop large-scale millimeter-wave mimo systems," *IEEE Transactions on Wireless Communications*, vol. 16, no. 7, pp. 4770–4785, 2017.

[21] K. Jo, M. Lee, J. Kim, and M. Sunwoo, "Tracking and behavior reasoning of moving vehicles based on roadway geometry constraints," *IEEE transactions on intelligent transportation systems*, vol. 18, no. 2, pp. 460–476, 2016.

This article has been accepted for publication in IEEE Transactions on Wireless Communications. This is the author's version which has not been fully edited and content may change prior to final publication. Citation information: DOI 10.1109/TWC.2023.3250442

15

[22] H. Wang, J. Kearney, and K. Atkinson, "Arc-length parameterized spline curves for real-time simulation," in *Proc. 5th International Conference on Curves and Surfaces*, vol. 387396, 2002.

[23] ——, "Robust and efficient computation of the closest point on a spline curve," in *Proceedings of the 5th International Conference on Curves and Surfaces*, 2002, pp. 397–406.

[24] H. Blom and Y. Bar-Shalom, "The interacting multiple model algorithm for systems with Markovian switching coefficients," *IEEE Transactions on Automatic Control*, vol. 33, no. 8, pp. 780–783, 1988.

[25] M. A. Richards, *Fundamentals of radar signal processing*. Tata McGraw-Hill Education, 2005.

[26] P. Stoica and A. Nehorai, "Music, maximum likelihood, and cramer-rao bound: further results and comparisons," *IEEE Transactions on Acoustics, Speech, and Signal Processing*, vol. 38, no. 12, pp. 2140–2150, 1990.

[27] L. Xu, J. Li, and P. Stoica, "Target detection and parameter estimation for MIMO radar systems," *IEEE Transactions on Aerospace and Electronic Systems*, vol. 44, no. 3, pp. 927–939, 2008.

[28] G. L. Erik, J. Li, and P. Stoica, *High-Resolution Nonparametric Spectral Analysis: Theory and Applications*. CRC Press, 2004, vol. 4.

[29] S. M. Kay, *Fundamentals of statistical signal processing: estimation theory*. Prentice-Hall, Inc., 1993.

[30] H. L. V. Trees, "Optimum array processing," 2002.

[31] B. G. M. E. Design and R. I. C. Ltd, *Code for design of urban road engineering CJJ 37-2012*, 1st ed., 1 2012.

Xiao Meng (Graduate Student Member, IEEE) received the BEng. degree from the Beijing Institute of Technology (BIT) in 2017, where he is currently pursuing the Ph.D. degree with the School of Integrated Circuits and Electronics. Since 2020, he has been a visiting student with the ISAC Lab, Department of Electronic and electrical engineering, Southern University of Science and Technology (SUSTech). His research interests include integrated sensing and communication systems, reconfigurable intelligent surfaces and precoding designs.

Fan Liu (Member, IEEE) is currently an Assistant Professor of the Department of Electronic and Electrical Engineering, Southern University of Science and Technology (SUSTech). He received the Ph.D. and the BEng. degrees from Beijing Institute of Technology (BIT), Beijing, China, in 2018 and 2013, respectively. He has previously held academic positions in the University College London (UCL), UK, first as a Visiting Researcher from 2016 to 2018, and then as a Marie Curie Research Fellow from 2018 to 2020.

Dr. Fan Liu's research interests lie in the general area of signal processing and wireless communications, and in particular in the area of Integrated Sensing and Communications (ISAC). He has 10 publications selected as IEEE ComSoc Besting Readings in ISAC. He is the Founding Academic Chair of the IEEE ComSoc ISAC Emerging Technology Initiative (ISAC-ETI), an Associate Editor for the IEEE Communications Letters and the IEEE Open Journal of Signal Processing, and a Guest Editor of the IEEE Journal on Selected Areas in Communications, IEEE Wireless Communications, and China Communications. He was also an organizer and Co-Chair for numerous workshops, special sessions and tutorials in flagship IEEE/ACM conferences, including ICC, GLOBECOM, ICASSP, and MobiCom. He is the TPC Co-Chair of the 2nd and 3rd IEEE Joint Communication and Sensing Symposium (JC&S), and will serve as a Track Co-Chair for the IEEE WCNC 2024. He is a Member of the IMT-2030 (6G) ISAC Task Group. He was the recipient of the IEEE Signal Processing Society Young Author Best Paper Award of 2021, the Best Ph.D. Thesis Award of Chinese Institute of Electronics of 2019, the EU Marie Curie Individual Fellowship in 2018, and has been named as an Exemplary Reviewer for IEEE TWC/TCOM/COMML for 5 times. Dr. Fan Liu was listed in the World's Top 2% Scientists by Stanford University for citation impact in 2021 and 2022.

Christos Masouros (Senior Member, IEEE) received the Diploma degree in Electrical and Computer Engineering from the University of Patras, Greece, in 2004, and MSc by research and PhD in Electrical and Electronic Engineering from the University of Manchester, UK in 2006 and 2009 respectively. In 2008 he was a research intern at Philips Research Labs, UK. Between 2009-2010 he was a Research Associate in the University of Manchester and between 2010-2012 a Research Fellow at Queen's University Belfast. In 2012 he joined University College London as a Lecturer. He has held a Royal Academy of Engineering Research Fellowship between 2011-2016.

He is currently a Full Professor in the Information and Communications Engineering research group, Dept. Electrical and Electronic Engineering, University College London. His research interests lie in the field of wireless communications and signal processing with particular focus on Green Communications, Large Scale Antenna Systems, Cognitive Radio, interference mitigation techniques for MIMO and multicarrier communications. He was the recipient of the Best Paper Awards in the IEEE GlobeCom 2015 and IEEE WCNC 2019 conferences, and has been recognised as an Exemplary Editor for the IEEE Communications Letters, and as an Exemplary Reviewer for the IEEE Transactions on Communications. He is an Editor for IEEE Transactions on Communications, and IEEE Transactions on Wireless Communications. He has been an Associate Editor for IEEE Communications Letters, and a Guest Editor for IEEE Journal on Selected Topics in Signal Processing issues "Exploiting Interference towards Energy Efficient and Secure Wireless Communications" and "Hybrid Analog / Digital Signal Processing for Hardware-Efficient Large Scale Antenna Arrays". He is currently an elected member of the EURASIP SAT Committee on Signal Processing for Communications and Networking.

Weijie Yuan (Member, IEEE) received the B.E. degree from the Beijing Institute of Technology, China, in 2013, and the Ph.D. degree from the University of Technology Sydney, Australia, in 2019. In 2016, he was a Visiting Ph.D. Student with the Institute of Telecommunications, Vienna University of Technology, Austria. He was a Research Assistant with the University of Sydney, a Visiting Associate Fellow with the University of Wollongong, and a Visiting Fellow with the University of Southampton, from 2017 to 2019. From 2019 to 2021, he was a Research Associate with the University of New South Wales. He is currently an Assistant Professor with the Department of Electrical and Electronic Engineering, Southern University of Science and Technology, Shenzhen, China.

Dr. Yuan currently serves as an Associate Editor for the IEEE Communications Letters, an Associate Editor as well as an Award Committee Member for the EURASIP Journal on Advances in Signal Processing. He has led the guest editorial teams for three special issues in IEEE Communications Magazine, IEEE Transactions on Green Communications and Networking, and China Communications. He was an Organizer/the Chair of several workshops, special sessions, and tutorials on orthogonal time frequency space (OTFS) and integrated sensing and communication (ISAC) in flagship IEEE and ACM conferences, including IEEE ICC, IEEE/CIC ICCC, IEEE SPAWC, IEEE VTC, IEEE WCNC, IEEE ICASSP, and ACM MobiCom. He is the Founding Chair of the IEEE ComSoc Special Interest Group on Orthogonal Time Frequency Space (OTFS-SIG). He was listed in the World's Top 2% Scientists by Stanford University for citation impact in 2022. He was a recipient of the Best Ph.D. Thesis Award from the Chinese Institute of Electronics, an Exemplary Reviewer Award from IEEE Transactions on Communications and IEEE Wireless Communications Letters, and a Best Editor Award from IEEE Communications Letters.
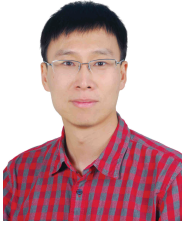
Qixun Zhang (Member, IEEE) received the B.Eng. degree in communication engineering and the Ph.D. degree in circuit and system from Beijing University of Posts and Telecommunications (BUPT), Beijing, China, in 2006 and 2011, respectively. From Mar. to Jun. 2006, he was a Visiting Scholar at the University of Maryland, College Park, Maryland. From Nov. 2018 to Nov. 2019, he was a Visiting Scholar in the Electrical and Computer Engineering Department at the University of Houston, Texas. He is a Professor with the Key Laboratory of Universal Wireless Communications, Ministry of Education, and the School of Information and Communication Engineering, BUPT. His research interests include B5G/6G mobile communication system, joint communication and sensing system for autonomous driving vehicle, mmWave communication system, cognitive radio and heterogeneous networks, game theory, and unmanned aerial vehicles (UAVs) communication. He is a member of IEEE and active in ITU-R WP5A/5C/5D standards.

Zhiyong Feng (Senior Member, IEEE) received her B.S., M.S., and Ph.D. degrees from Beijing University of Posts and Telecommunications (BUPT), Beijing, China. She is a Professor with the School of Information and Communication Engineering, BUPT, and the director of the Key Laboratory of Universal Wireless Communications, Ministry of Education, China. Her research interests include joint communication and sensing system design, wireless network architecture design and radio resource management, spectrum sensing and dynamic spectrum management in cognitive wireless networks, universal signal detection and identification, and network information theory. She is a senior member of IEEE and active in standards development, such as ITU-R WP5A/5C/5D, IEEE 1900, ETSI, and CCSA.